ROYAL SOCIETY OF CHEMISTRY

PAPER

Check for updates

Dynamic self-regulating interfaces enable crystallization control and lead sequestration in perovskite photovoltaics

Wenhui Meng, Haojie Sui, Zan Li, Xinjing Chen, Yongjia Li, Shufang Zhang, [ID] *
Hai Zhong, Qi Zhang and Changlin Yao*

Carbon-electrode, hole-transport-layer-free perovskite solar cells (C-PSCs) offer compelling commercialization potential but suffer from uncontrolled crystallization, leading to defective films and severe non-radiative losses. Current interfacial modifications passively form adducts, failing to kinetically regulate crystallization. This work pioneers a dynamic, self-regulating interface strategy using nickel acetate (NA). NA enables *in situ* generation of a Pb^{2+} complex reservoir *via* reversible ion exchange (PbI_2 + Ni $(CH_3COO)_2 \rightleftharpoons Pb(CH_3COO)_2 + NiI_2$). The controlled Pb^{2+} release from the complex reservoir uniquely achieves dual functionality: it kinetically suppresses nucleation for large-grained films while simultaneously passivating interfacial defects. This synergistic action, coupled with optimized energy-level alignment, yields significantly enhanced charge extraction. Consequently, NA-modified C-PSCs achieve a record power conversion efficiency (PCE) of 18.43% (*vs.* 14.11% for the control) with exceptional operational stability. Crucially, the synergistic action of chemical bonding in the insoluble Pb–Ni complex and the physical barrier formed by the NiO_x layer during annealing drastically reduces lead leakage, establishing a dual-function paradigm for highly efficient, stable, and eco-compatible perovskite photovoltaics.

1. Introduction

Perovskite solar cells (PSCs) exhibit compelling commercialization potential due to their solution processability, superior light absorption coefficients, and tunable bandgaps (1.5–2.3 eV).[1–6] Planar hole-transport-layer-free perovskite solar cells (PSCs) offer significant advantages by eliminating the unstable hole transport layer (*e.g.*, Spiro-OMeTAD or PTAA) and the high-temperature-processed, interface-sensitive mesoporous layer (*e.g.*, ZrO_2 or carbon), making them a highly promising architecture for future development.[7–9] However, rapid crystallization kinetics in these systems generates small-grained films with excessive residual PbI_2 and multi-scale defects, severely aggravating non-radiative recombination.[10–13] These limitations critically constrain power conversion efficiencies and operational stability, impeding commercial deployment.[14,15] Precise crystallization control is therefore decisive for advancing high-performance, industrially viable perovskite photovoltaics.[16–19]

Recent advances in perovskite photovoltaics have witnessed extensive exploration of interfacial modifiers, including organic small molecules, polymeric materials, and inorganic salts.[20–23] For instance, Tan *et al.* introduced potassium sucrose octasulfate (K_8SOS) through multipoint enhanced chemical bonding to bridge the SnO_2/perovskite buried interface, passivate defects in the perovskite and SnO_2, suppress non-radiative recombination and ion migration, improve the crystallinity of perovskite layers, and achieve a high efficiency of 25.32%.[24] Cao *et al.* used phenylhydrazinium chloride (PC) as a passivator to reduce defect density and delay the crystallization process of perovskite films. The PCE of small area devices can reach 25.80%.[25] Zhang *et al.* used a guanidine salt passivator (Agu) to improve the SnO_2/perovskite interface and utilized the enhanced hydrophobicity of the heterojunction interface of hydrogen bond sites to increase the perovskite grain size, achieving a reduction in trap density and non-radiative recombination, and the PSCs achieved a 24.4% PCE.[26] While current interfacial modifications rely passively on adduct formation between modifiers and perovskite precursors, yielding limited crystallization improvement, they fail to achieve kinetic control over nucleation and growth.[27,28] This fundamental limitation perpetuates heterogeneous crystallization and defect proliferation.

Herein, we pioneer a dynamic, self-regulating interface strategy employing nickel acetate (NA) to *in situ* generate a Pb^{2+} complex reservoir *via* reversible ion exchange (PbI_2 +

School of Physics and Photoelectronic Engineering, Ludong University, Yantai, 264025, China. E-mail: zhang.shufang@ldu.edu.cn, cyao1992@ldu.edu.cn

$Ni(CH_3COO)_2 \rightleftharpoons Pb(CH_3COO)_2 + Ni_2$). The controlled Pb^{2+} release from $Pb(CH_3COO)_2$ kinetically suppresses nucleation while simultaneously passivating interfacial defects, enabling large-grained, low-trap-density perovskite films. Concurrently, optimized energy-level alignment enhances charge extraction. Consequently, NA-modified carbon-electrode, HTL-free PSCs achieve a record PCE of 18.43% (J_{SC} = 22.71 mA cm^{-2}, V_{OC} = 1.11 V, FF = 73.1%), surpassing control devices (14.11% PCE) with exceptional stability. The synergistic effect between the chemically bonded insoluble Pb–Ni complex and the NiO$_x$ physical barrier is crucial, as it significantly suppresses lead leakage and introduces a dual-functional strategy for developing efficient, stable, and environmentally compatible perovskite photovoltaics.

2. Results and discussion

During the crystallization of perovskite films, excess lead iodide (PbI$_2$) accumulated at the interface accelerates crystal growth kinetics, resulting in small, heterogeneous grains and residual PbI$_2$ that act as charge recombination centers, causing significant energy losses.[29,30] To address this issue, we introduce nickel acetate (NA) as an interfacial modifier between the electron transport layer (ETL) and the perovskite. Leveraging Le Chatelier's principle, a spontaneous ion-exchange reaction occurs (Fig. 1a): PbI$_2$ + Ni(CH$_3$COO)$_2$ ⇌ Pb(CH$_3$COO)$_2$ + NiI$_2$. This reaction generates an insoluble Pb(CH$_3$COO)$_2$–NiI$_2$ complex at the ETL interface (Fig. S1).[31] In the XPS spectra (Fig. S2 and S3), the Pb 4f peaks of pristine PbI$_2$ shifted negatively from 144.35 eV and 139.49 eV to 143.73 eV and 138.91 eV after mixing with NA and drying.

Concurrently, the Ni 2p peak shifted to higher binding energy compared to pure NA. The C=O stretching vibration of NA red-shifted from 1583 cm^{-1} to 1571 cm^{-1} upon binding with PbI$_2$ (Fig. S4), confirming the formation of a bimetallic complex. During thermal annealing, the complex gradually releases Pb^{2+} ions, reducing supersaturation and enabling complete reaction with AX (FAI or MAI/CsI), thereby decelerating perovskite crystallization.[32] To elucidate the mechanism, we performed density functional theory (DFT) calculations to analyze the molecular electrostatic potential (ESP) of NA.[30,33] As shown in Fig. 1b, Ni^{2+} exhibits a positive ESP, while the carbonyl group displays a pronounced negative potential, indicating strong charge delocalization, a prerequisite for ion exchange.

To validate the reaction pathway, we computed the binding energies between acetate ions and Pb^{2+}/Ni^{2+} using reduced density gradient (RDG) analysis. Fig. 1c and d reveal distinct blue regions (strong attraction) between Pb^{2+} and acetate, contrasting with weaker interactions for Ni^{2+}. Critically, the binding energy for Pb^{2+}-acetate (Fig. 1e and f) is −2.38 eV, which is lower than that of Ni^{2+}-acetate (−0.34 eV), confirming the preferential formation of Pb(CH$_3$COO)$_2$. This facilitates the formation of a uniform, dense Pb(CH$_3$COO)$_2$ layer on the ETL surface, ultimately regulating perovskite growth. The optimized crystallization process is schematically illustrated in Fig. 1g.

Surface morphology analysis *via* SEM (Fig. 2a and b) reveals uniformly distributed SnO$_2$ grains on both pristine and NA-modified substrates, confirming that NA treatment induces no adverse effects on the ETL microstructure. Optical characterization (Fig. 2c and Fig. S5, S6) further demonstrates negligible differences in transmittance and absorbance spectra, indicating that the NA interlayer does not compromise light harvest-
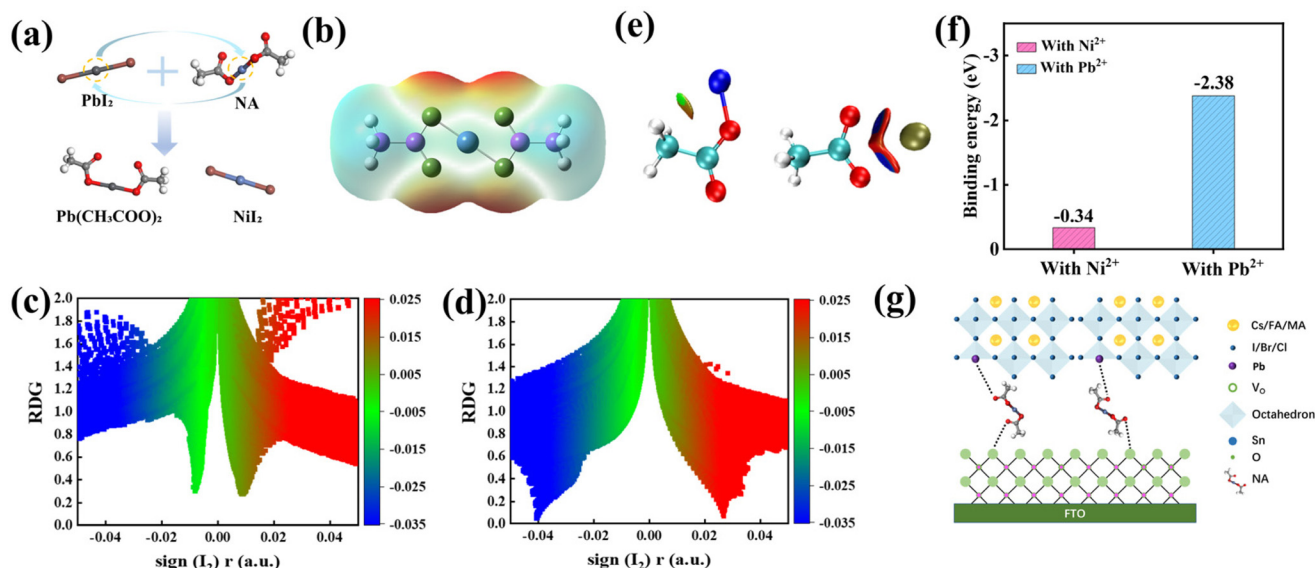

Fig. 1 (a) Ion exchange reaction diagram. (b) Electrostatic diagram of the NA surface. Two-dimensional scatter plots of RDG for NA molecules with (c) Ni^{2+} and (d) Pb^{2+}. (e) Three-dimensional RDG isosurface diagrams of NA molecules with Ni^{2+} and Pb^{2+}. (f) Binding energy of different components. (g) Mechanism diagram.
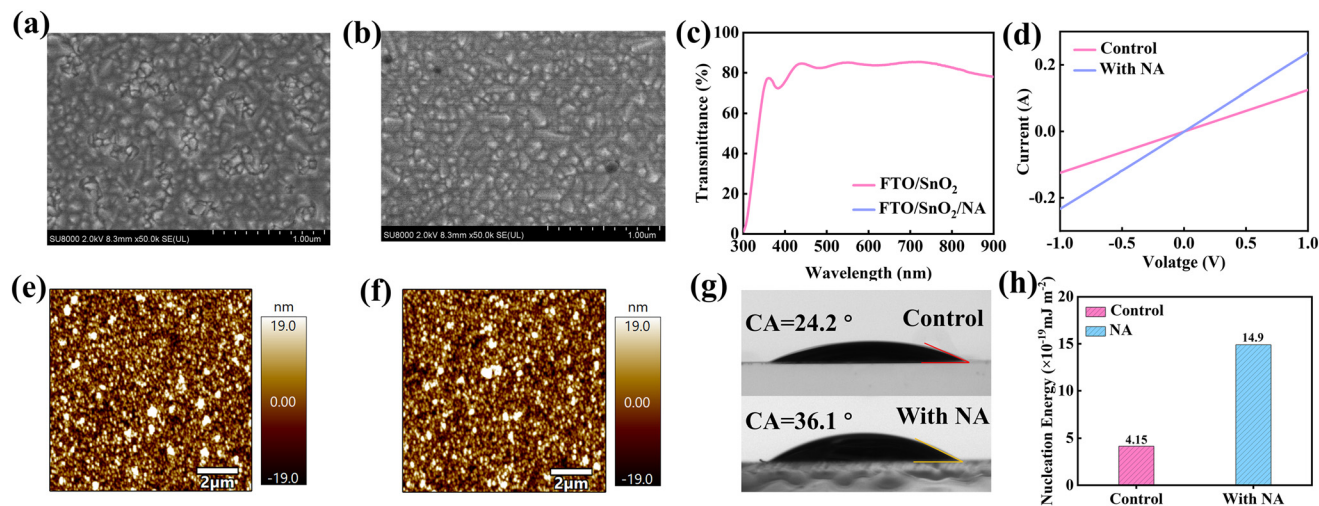
Fig. 2 SEM images of (a) SnO$_2$ and (b) SnO$_2$/NA. (c) Transmission spectra of different SnO$_2$ ETL thin films. (d) I–V curves of different SnO$_2$ ETL films. (e) and (f) AFM images of the SnO$_2$ film and the SnO$_2$/NA film. The (g) water contact angle and (h) nucleation work of SnO$_2$ thin films with original and NA modification.

ing in the perovskite layer. Critically, electrical conductivity measurements (Fig. 2d) show that NA modification enhances SnO$_2$ conductivity from 0.18 to 0.23 S m^{-1}. We attribute this improvement to acetate-induced passivation of surface oxygen vacancies, which reduces trap-assisted recombination and facilitates charge extraction.[34]

Atomic force microscopy (AFM) quantifies the interfacial contact quality: the root-mean-square (RMS) roughness decreases from 9.50 nm (pristine SnO$_2$) to 8.44 nm (NA-modified), as shown in Fig. 2e and f. This smoother surface enhances ETL/perovskite interfacial adhesion, promoting carrier transfer while enabling uniform spreading of PbI$_2$ precursor solutions, a prerequisite for complete conversion to dense PbAc$_2$ films during ion exchange.[35] Contact angle measurements (Fig. 2g and h) provide mechanistic insights into crystallization control: NA modification increases the contact angle of perovskite precursors from 24.2° to 36.1°. Applying the Young–Dupré equation and classical nucleation theory, we calculate a higher nucleation energy barrier ($\gamma = 1.49 \times 10^{-18}$ mJ m^{-2}) on NA-treated surfaces *versus* the control ($\gamma = 4.15 \times 10^{-19}$ mJ m^{-2}). This suppressed nucleation kinetics favors the growth of large-grained perovskite films.[36] The nickel salt forms a NiO$_x$ layer during annealing, which acts as a physical barrier that inhibits the release of Pb^{2+} ions, thereby further delaying the crystallization process of perovskite films. In addition, as illustrated in Fig. S7 and S8, the introduction of nickel acetate (NA) into the perovskite precursor solution results in a larger colloidal particle size (increasing from 131.1 nm to 159.5 nm) and a higher zeta potential (rising from 3.82 mV to 7.13 mV). This change can be attributed to the strong coordination between acetate and the precursor, which promotes the formation of larger colloids. These optimized colloidal characteristics contribute to the growth of perovskite films with larger grain sizes and improved morphology. *In situ*

UV-vis tracking of perovskite films during thermal annealing (Fig. 3a and b) reveals that NA-modified samples exhibit slower absorption evolution kinetics in the initial phase compared to the control. This delayed optical response confirms retarded crystallization kinetics, attributed to the gradual release of Pb^{2+} ions from the interfacial layer. Such controlled growth enables the formation of highly compact, large-grained perovskite films with suppressed defect formation.[37]

Surface morphology analysis (Fig. 3c and d) reveals that perovskite films deposited on NA-modified SnO$_2$ ETLs exhibit enlarged grain sizes (from 418.9 nm to 718.4 nm, as shown in Fig. S9) and suppressed pinhole formation, confirming effective crystallization regulation through controlled Pb^{2+} release. This aligns with XRD patterns (Fig. 3e), where NA-treated films demonstrate enhanced perovskite phase peak intensities (14.1°, 28.4°) and near-complete suppression of PbI$_2$ signals (12.4°), verifying minimized residual PbI$_2$ formation *via* delayed reaction kinetics. It is noticeable that the FWHM value of the (110) peak after NA modification was 0.072°, which was lower than the control film (0.082°) (Fig. S10), which is consistent with the SEM results, further proving that NA treatment improves the quality of perovskite films.[28] Optoelectronic characterization further corroborates improved film quality: (i) UV-vis spectra (Fig. 3f) show absorption enhancement in the 500–800 nm range, directly contributing to potential J_{SC} gains; (ii) Tauc plots (Fig. 3g) indicate negligible bandgap alterations, excluding electronic structure modifications; (iii) AFM quantification (Fig. 3h and i) documents reduced RMS roughness from 22.3 nm (pristine) to 14.7 nm (NA-treated), mitigating interfacial recombination through improved interfacial contact.

To evaluate the impact of NA treatment on photovoltaic performance, carbon-based HTL-free PSCs with an FTO/SnO$_2$/perovskite/carbon architecture (Fig. 4a) were fabricated. Current
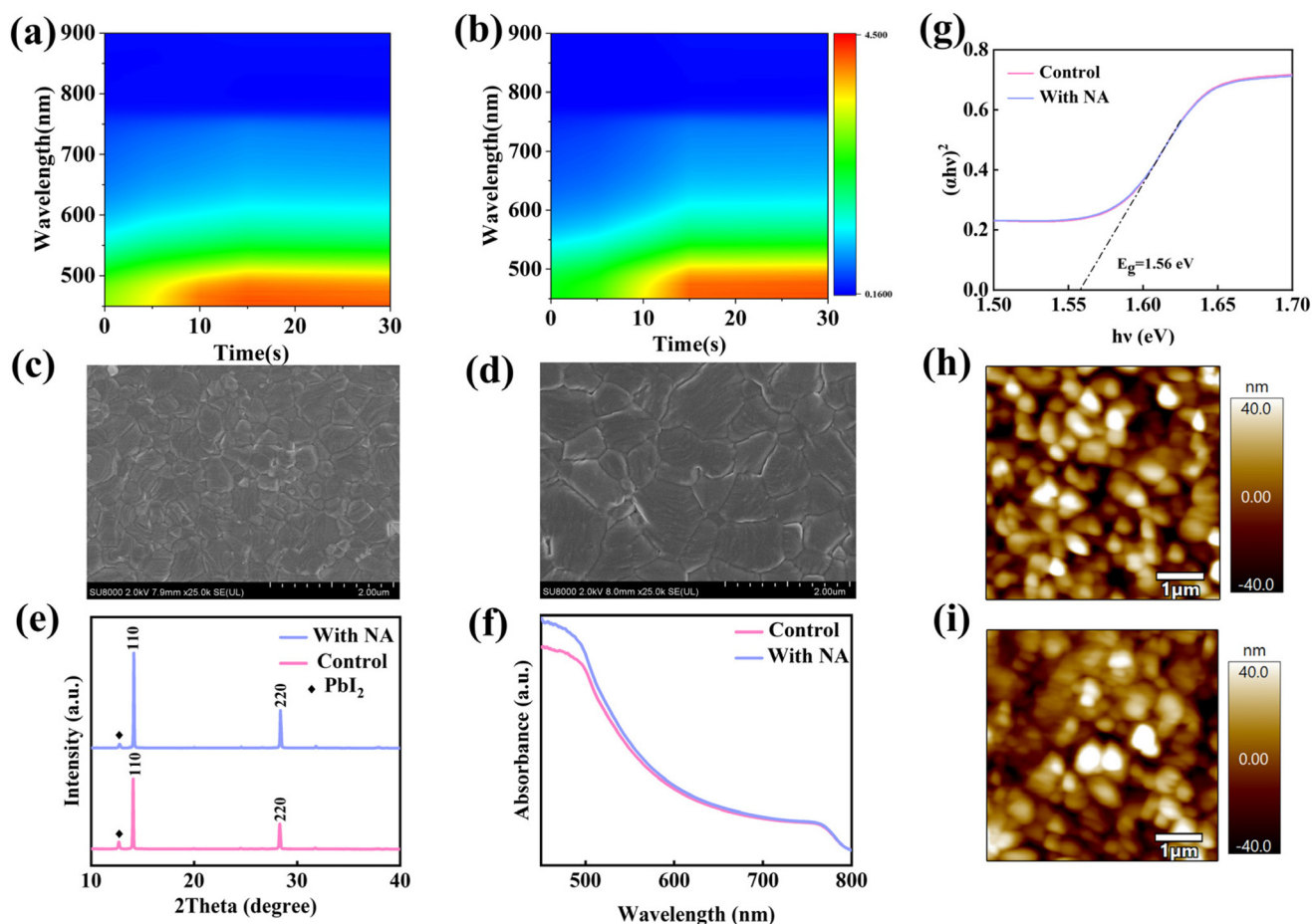
Fig. 3 2D UV-vis spectra of perovskite thin films prepared with (a) original and (b) NA-modified SnO₂ at different annealing times. SEM images of (c) SnO₂/PVK and (d) SnO₂/NA/PVK. (e) XRD patterns, (f) UV-vis patterns, and (g) Tauc plots of perovskite thin films prepared with original and NA-modified SnO₂. AFM images of (h) SnO₂/PVK and (i) SnO₂/NA/PVK.

density–voltage (J–V) measurements under AM 1.5G illumination (100 mW cm^{-2}) reveal that devices modified with 0.25 mg mL^{-1} NA achieve a champion PCE of 18.43% (J_{SC} = 22.71 mA cm^{-2}, V_{OC} = 1.11 V, FF = 73.1%), representing a record efficiency for carbon-electrode PSCs and substantially exceeding the control device's PCE of 14.11% (Fig. 4b), and the photovoltaic parameters are shown in (Fig. 4b and Table S1). This enhancement primarily arises from NA-induced film quality improvement and interfacial contact optimization. Steady-state power output at the maximum power point (Fig. 4c) confirms negligible degradation over 500 s of operation. Further validation comes from the increased integrated J_{SC} (Fig. 4d), rising from 20.13 to 22.39 mA cm^{-2}, demonstrating excellent agreement with J–V values and affirming device reliability. In addition, the box plots of PCE for 20 original devices and C-PSCs modified with NA were analyzed under the same conditions, and the corresponding standard deviations were calculated (Fig. S11). Compared with the original device, the PCE of the NA-modified device is more concentrated and the average value is higher, further proving that NA-modified C-PSCs have better performance reproducibility and reliability.

Ultraviolet photoelectron spectroscopy (UPS) analysis (Fig. 4e and f) reveals a positive shift in both valence band (VB) and conduction band (CB) energies for NA-modified perovskite films, using the formula: $E_V = E_F - E_{onset}$, $E_F = E_{cutoff} - 21.22$ eV and $E_C = E_V + E_g$, where E_F, E_{onset} and E_{cutoff} are the Fermi level, onset binding energy and secondary electron cutoff energy, calculated as −5.63 eV (VB) and −4.07 eV (CB) versus −5.80 eV (VB) and −4.24 eV (CB) for the control. This alignment optimization, illustrated in the energy-level diagram (Fig. 4g) from each phase, reduces the hole extraction barrier at the perovskite/carbon electrode interface to 0.63 eV, directly contributing to enhanced V_{OC}.[38] Photoluminescence studies (Fig. 4h) demonstrate obvious PL quenching in NA-modified devices (FTO/SnO₂/NA/perovskite), attributed to suppressed interfacial recombination through defect passivation, thereby facilitating the transfer of carriers. Time-resolved PL (Fig. 4i and Table S2) corroborates accelerated charge extraction, with the average carrier lifetime (τ_{avg}) decreasing from 25.18 ns (pristine) to 17.75 ns (NA-treated), consistent with improved interfacial contact quality.[39]
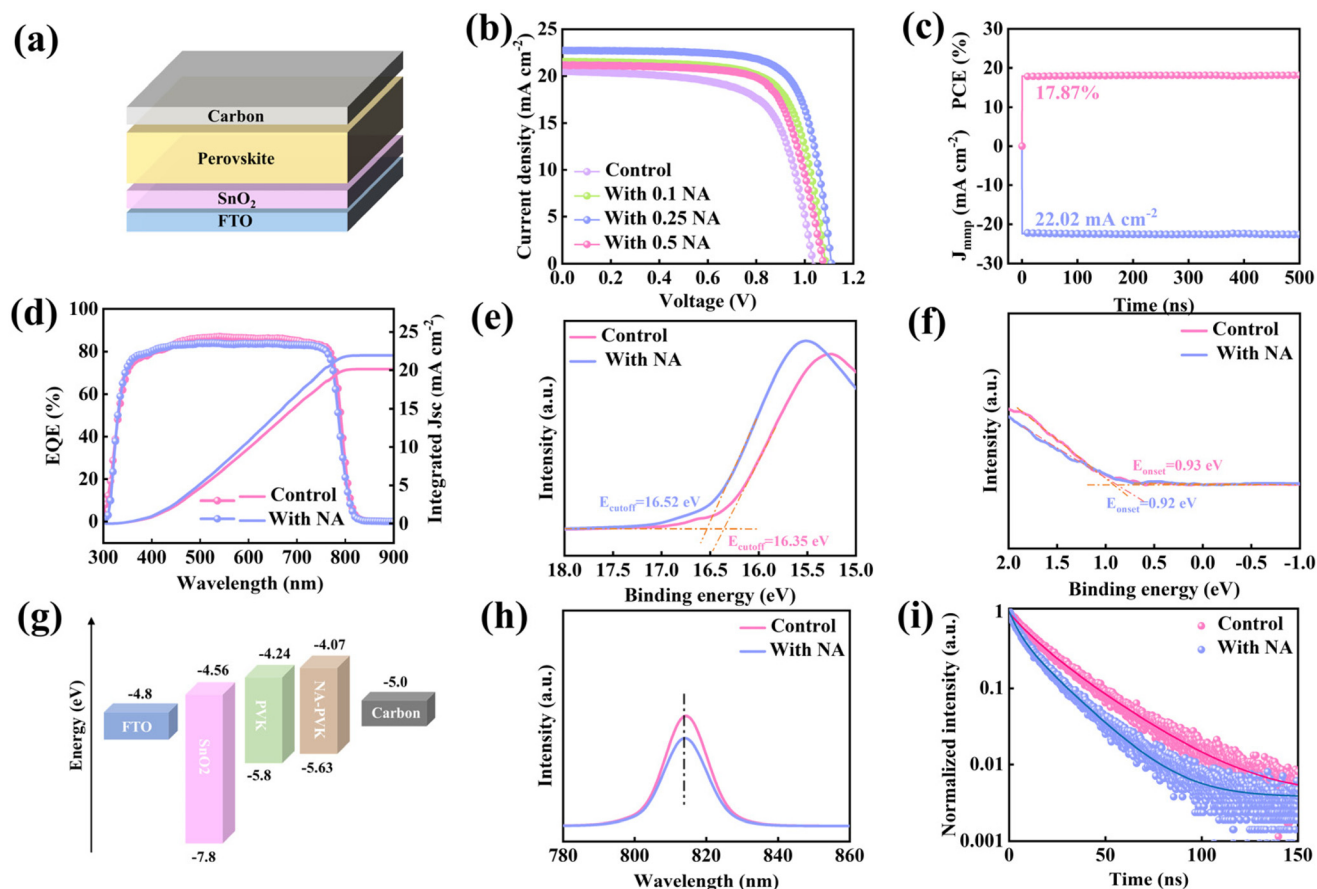
Fig. 4 (a) A schematic diagram of the carbon-based HTL-free PSC. (b) J–V curves of champion PSCs modified with original and different concentrations of NA. (c) The steady-state power output of the optimal device at the maximum power point. (d) Original and NA-modified EQE spectra. (e) and (f) UPS diagram and of perovskite thin films prepared from raw and NA-modified SnO_2. (g) Energy level diagram of different C-PSCs. (h) The steady-state PL spectra and (i) TRPL curves of $FTO/SnO_2/PVK$ and $FTO/SnO_2/NA/PVK$.

Electrochemical characterization reveals significantly improved charge transport kinetics in NA-modified devices. Dark current–voltage measurements (Fig. 5a) demonstrate reduced leakage current in NA-treated devices, indicating suppressed non-radiative recombination through enhanced film quality and ETL/perovskite interface passivation.[40] Voltage-light intensity dependence analysis (Fig. 5b) yields an ideality factor of $n = 1.36$ kT/q for NA-modified devices *versus* 1.75 kT/q for controls, confirming reduced trap-assisted recombination that directly enhances V_{OC} and FF.[41] Space-charge-limited-current (SCLC) measurements of electron-only devices (FTO/SnO_2/(with/without)NA/perovskite/PCBM/carbon, Fig. 5c and d) quantify defect density reduction using: $N_{trap} = 2\varepsilon_r\varepsilon_0 V_{TFL}/eL^2$, where ε_r is the relative permittivity, ε_0 is the vacuum permittivity, L is the film thickness, and V_{TFL} is the trap-fill limit voltage. NA modification reduces N_{trap} from 1.79×10^{15} cm^{-3} ($V_{TFL} = 0.22$ V) to 1.03×10^{15} cm^{-3} ($V_{TFL} = 0.16$ V), validating defect suppression that synergistically minimizes non-radiative losses.[42] Furthermore, PL measurements were performed on Glass/PVK samples (Fig. S12). The NA-treated perovskite films exhibited a significant enhancement in PL intensity along with a blue shift of the emission peak, indicating effective defect

passivation and suppressed non-radiative recombination.[40] Electrochemical impedance spectroscopy (EIS, Fig. 5e and Table S3) reveals that NA-modified devices exhibit reduced transfer resistance ($R_{tr} = 7398.4$ Ω) and enhanced recombination resistance ($R_{rec} = 8.44 \times 10^6$ Ω) compared to control values ($R_{tr} = 8199.5$ Ω, $R_{rec} = 7.35 \times 10^6$ Ω). This dual improvement signifies suppressed non-radiative recombination and accelerated charge transport, directly contributing to enhanced J_{SC} and V_{OC}.[43] Mott–Schottky analysis (Fig. 5f) further demonstrates a strengthened built-in potential (V_{bi}) of 1.02 V for NA-treated devices *versus* 1.06 V for controls, with steeper curve slopes confirming mitigated interfacial charge accumulation and improved charge separation efficiency.

Device stability and environmental safety are critical for perovskite solar cell commercialization. NA modification increases the water contact angle from 55.7° to 77.1° (Fig. 6a), demonstrating enhanced moisture resistance through enlarged grain hydrophobicity. Unencapsulated devices aged at 25 °C/40% RH in the dark retain 90% of the initial PCE after 1000 hours (Fig. 6b), significantly outperforming controls (62% retention). Under continuous one-sun illumination under an N_2 atmosphere and open circuit (Fig. 6c) conditions,
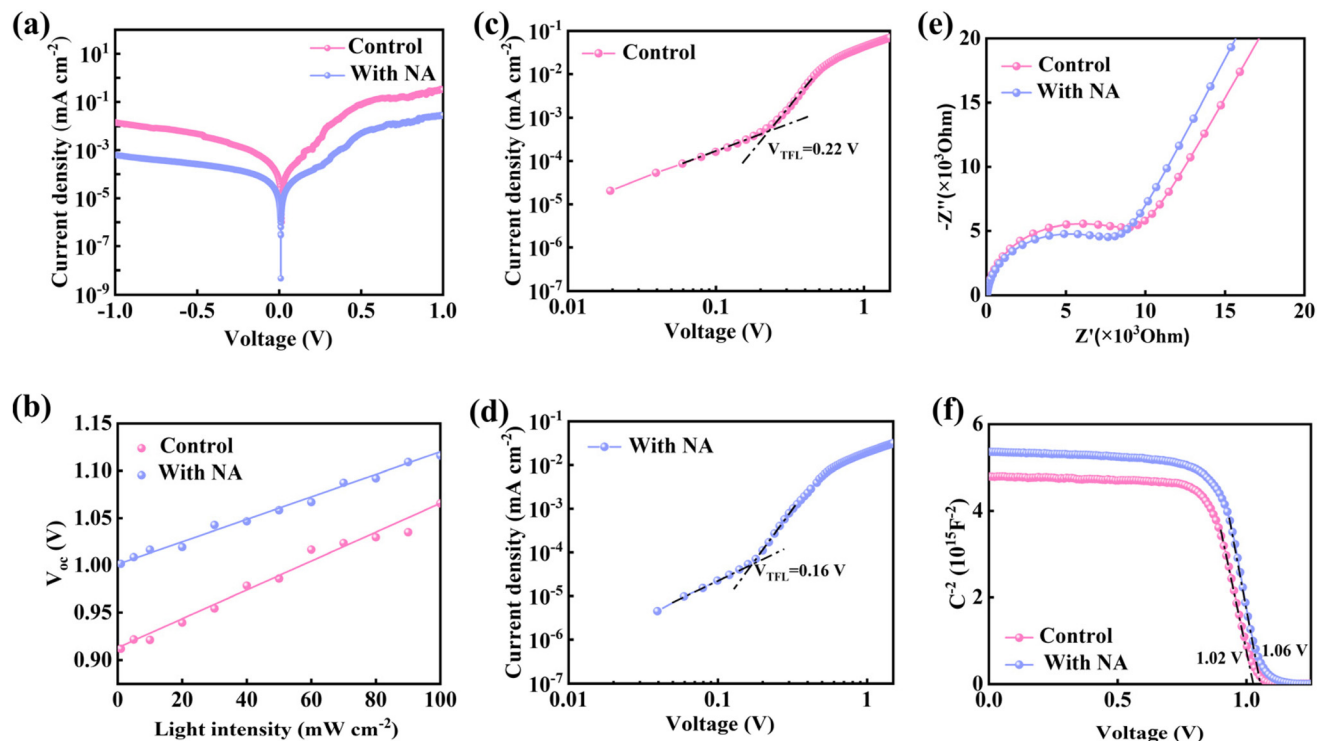
Fig. 5 (a) Dark state *J*−*V* curves of different PSCs. (b) *V*_OC−*I* curves and their fitting curves. (c and d) *J*−*V* curves measured by the SCLC method. (e) Nyquist curves. (f) Mott−Schottky (MS) curves.
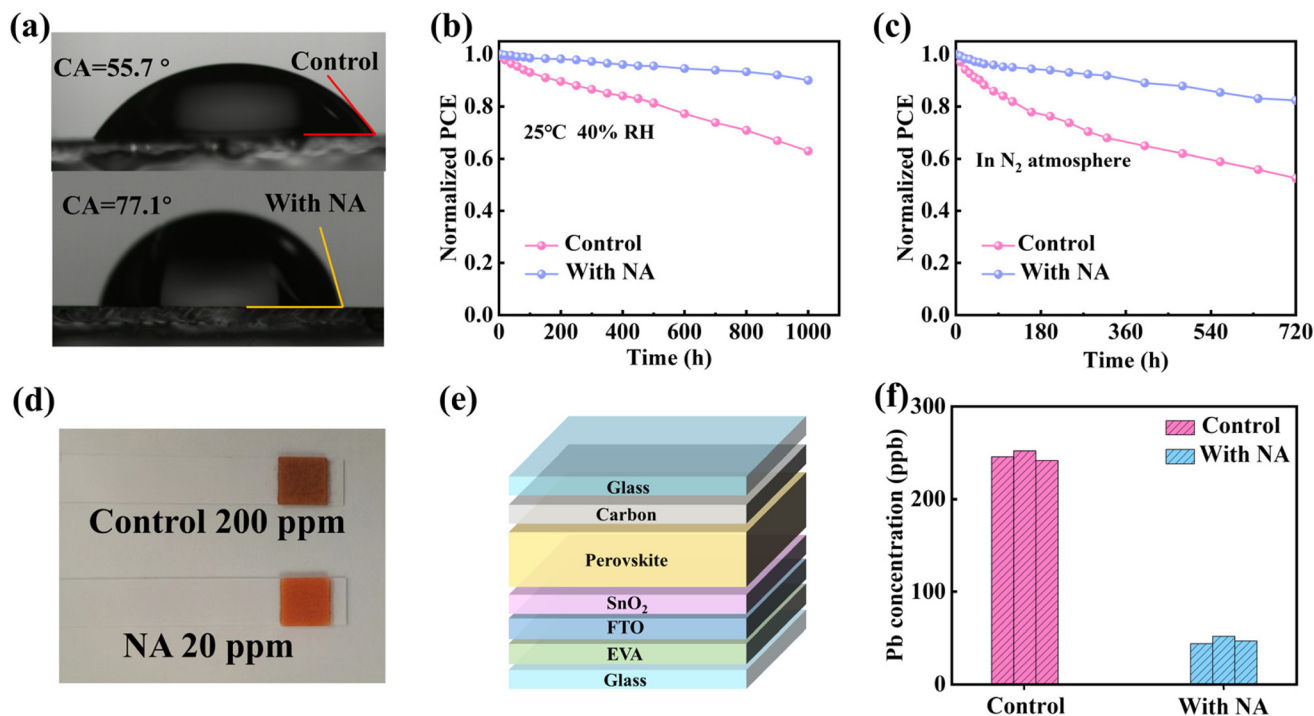

Fig. 6 (a) Water contact angles of perovskite films prepared with original and NA-modified SnO$_2$. (b) Long term stability of different PSCs in 25 °C and 40% RH environments. (c) Long term stability of different PSCs in a N$_2$ glove box. (d) Comparison chart of Pb^{2+} test strips. (e) Schematic diagram of the PSCs encapsulated with EVA and glass. (f) The detected lead concentration in polluted water by inductively coupled plasma-optical emission spectroscopy (ICP-OES) measurements.

NA-optimized PSCs maintain 82% PCE after 720 hours *versus* rapid control degradation (52% retention). This stability enhancement originates from NA-induced defect passivation and improved film compactness.

Furthermore, systematic lead sequestration analysis confirms NA's efficacy in suppressing Pb^{2+} leakage and immobilizing Pb^{2+}. Colorimetric tests in saturated lead solutions demonstrate that NA-induced reduction of Pb^{2+} (Fig. 6d) is attributed to the chemical binding of the insoluble Pb–Ni complex and the physical barrier effect of the NiO_x layer. To evaluate real-world environmental risks, hail-damaged devices were encapsulated with EVA/glass on the silver electrode side (Fig. 6e), tilted at 30°, and subjected to deionized water flow (5 mL h^{-1} for 1 h; Fig. S13).[44,45] ICP-OES quantification reveals NA-modified devices reduce Pb^{2+} leakage from 49 ppb to 252 ppb (Fig. 6f), outperforming conventional encapsulation strategies.

3. Conclusion

This work establishes a paradigm-shifting dynamic self-regulating interface through reversible ion exchange between nickel acetate and interfacial PbI_2 ($PbI_2 + Ni(CH_3COO)_2 \rightleftharpoons Pb(CH_3COO)_2 + NiI_2$). The *in situ* generated $Pb(CH_3COO)_2$ reservoir enables: (1) kinetically controlled crystallization yielding large-grained, low-trap-density films, (2) dual passivation of SnO_2 oxygen vacancies and perovskite defects, and (3) reduction of Pb^{2+} leakage (49 ppb). These innovations deliver carbon-electrode PSCs with a record 18.43% PCE with unprecedented stability. Crucially, the system transcends conventional strategies by synchronizing crystallization control, efficiency optimization, and eco-safety through a single dynamically regulated interface. This work provides a blueprint for sustainable commercialization of perovskite photovoltaics, resolving the critical efficiency–stability–environment trilemma.

Conflicts of interest

The authors declare no competing financial interest.

Data availability

All data required to reproduce the findings of this study are included in the supplementary information (SI). No external repositories were used.

Acknowledgements

References

1 C. M. Sutter-Fella, Y. B. Li, M. Amani, J. W. Ager, F. M. Toma, E. Yablonovitch, I. D. Sharp and A. Javey, *Nano Lett.*, 2016, **16**, 800–806.

2 G. Yang, Z. W. Ren, K. Liu, M. C. Qin, W. Y. Deng, H. K. Zhang, H. B. Wang, J. W. Liang, F. H. Ye, Q. Liang, H. Yin, Y. X. Chen, Y. L. Zhuang, S. Q. Li, B. W. Gao, J. B. Wang, T. T. Shi, X. Wang, X. H. Lu, H. B. Wu, J. H. Hou, D. Y. Lei, S. K. So, Y. Yang, G. J. Fang and G. Li, *Nat. Photonics*, 2021, **15**, 681–689.

3 L. Y. Yue, B. Yan, M. Attridge and Z. B. Wang, *Sol. Energy*, 2016, **124**, 143–152.

4 M. H. Miah, M. U. Khandaker, M. B. Rahman, M. Nur-E-Alam and M. A. Islam, *RSC Adv.*, 2024, **14**, 15876–15906.

5 S. Sánchez, L. Pfeifer, N. Vlachopoulos and A. Hagfeldt, *Chem. Soc. Rev.*, 2021, **50**, 7108–7131.

6 Y. M. Liu, Z. Y. Zhang, T. H. Wu, W. X. Xiang, Z. Z. Qin, X. Q. Shen, Y. Peng, W. Z. Shen, Y. F. Li and L. Y. Han, *Nano-Micro Lett.*, 2025, **17**, 219.

7 X. N. Huo, J. Q. Lv, K. X. Wang, W. W. Sun, W. F. Liu, R. Yin, Y. S. Sun, Y. K. Gao, T. T. You and P. G. Yin, *Carbon Energy*, 2024, **6**, 12.

8 X. Li, Y. Tan, H. Lai, S. P. Li, Y. Chen, S. W. Li, P. Xu and J. Y. Yang, *ACS Appl. Mater. Interfaces*, 2019, **11**, 29746–29752.

9 J. W. Zhu, M. X. Tang, B. L. He, K. X. Shen, W. Y. Zhang, X. M. Sun, M. R. Sun, H. Y. Chen, Y. Y. Duan and Q. W. Tang, *Chem. Eng. J.*, 2021, **404**, 10.

10 H. K. Guo, F. H. Hou, X. L. Ning, X. Q. Ren, H. R. Yang, R. Liu, T. T. Li, C. J. Zhu, Y. Zhao, W. Li and X. D. Zhang, *J. Energy Chem.*, 2024, **91**, 313–322.

11 T. X. Zhou, X. Huang, D. Zhang, W. Liu and X. A. Li, *Nanomaterials*, 2024, **14**, 10.

12 D. Y. Luo, R. Su, W. Zhang, Q. H. Gong and R. Zhu, *Nat. Rev. Mater.*, 2020, **5**, 44–60.

13 J. M. Ball and A. Petrozza, *Nat. Energy*, 2016, **1**, 1–13.

14 M. J. Grotevent, Y. L. Lu, T. Sverko, M. C. Shih, S. Tan, H. Zhu, T. Dang, J. K. Mwaura, R. Swartwout, F. Beiglböck, L. Kothe, V. Bulovic and M. G. Bawendi, *Adv. Energy Mater.*, 2024, **14**, 8.

15 X. Y. Wang, Y. Zhong, Y. K. Liu, X. Luo, B. L. Gao, L. C. Tan and Y. W. Chen, *Angew. Chem., Int. Ed.*, 2025, **64**, 11.

16 L. X. Zeng, S. Chen, K. Forberich, C. J. Brabec, Y. H. Mai and F. Guo, *Energy Environ. Sci.*, 2020, **13**, 4666–4690.

17 C. Yang, W. J. Hu, J. L. Liu, C. Z. Han, Q. J. Gao, A. Y. Mei, Y. H. Zhou, F. W. Guo and H. W. Han, *Light:Sci. Appl.*, 2024, **13**, 48.

18 P. Wang, Y. H. Wu, B. Cai, Q. S. Ma, X. J. Zheng and W. H. Zhang, *Adv. Funct. Mater.*, 2019, **29**, 37.

19 C. Y. Wang, J. W. Xiang, J. L. Liu, C. Z. Han, Z. W. Zheng, M. H. Xia, S. Shen, Z. Z. Cui, X. R. Wang, J. Y. Xie, X. Y. Li, A. Y. Mei, Y. Zhou and H. W. Han, *Adv. Mater.*, 2025, **37**, 2502724.

20 M. Vasilopoulou, A. Fakharuddin, A. G. Coutsolelos, P. Falaras, P. Argitis, A. R. B. Yusoff and M. K. Nazeeruddin, *Chem. Soc. Rev.*, 2020, **49**, 4496–4526.

21 S. Q. Bi, X. Y. Leng, Y. X. Li, Z. Zheng, X. N. Zhang, Y. Zhang and H. Q. Zhou, *Adv. Mater.*, 2019, **31**, 8.

22 H. Y. Zhang, Y. M. Li, S. Tan, Z. J. Chen, K. K. Song, S. X. Huang, J. J. Shi, Y. H. Luo, D. M. Li and Q. B. Meng, *J. Colloid Interface Sci.*, 2022, **608**, 3151–3158.

23 G. P. Huang, T. Y. Zhang, W. D. Lin, L. X. Qin, S. Z. Kang and X. Q. Li, *Angew. Chem., Int. Ed.*, 2025, **64**, e202420687.

24 H. T. Tan, X. Yu, W. B. Ren, T. Z. Yin, H. X. Wen, Y. X. Guo, Z. M. Zhang, C. P. Liu, G. S. Zhou, H. Li, X. J. Qiu, H. L. Wu, Z. Yang and S. M. Huang, *Small*, 2025, **21**, 9.

25 Y. Cao, L. Yang, N. Yan, L. Meng, X. Chen, J. Zhang, D. Qi, J. Pi, N. Li, X. Feng, C. Ma, F. Xiao, G. Zhao, S. Tan, X. Liu, Y. Liu, K. Zhao, S. F. Liu and J. Feng, *Energy Environ. Sci.*, 2025, **18**, 1659–3667.

26 B. Zhang, J. Oh, Z. Sun, Y. Cho, S. Jeong, X. Chen, K. Sun, F. Li, C. D. Yang and S. S. Chen, *ACS Energy Lett.*, 2023, **8**, 1848–1856.

27 Z. H. Zhang, Z. H. Su, G. X. Li, J. Li, M. H. Aldamasy, J. X. Wu, C. Y. Wang, Z. Li, X. Y. Gao, M. Li and A. Abate, *Adv. Funct. Mater.*, 2024, **34**, 9.

28 J. J. Ma, M. C. Qin, P. W. Li, L. Y. Han, Y. Q. Zhang and Y. L. Song, *Energy Environ. Sci.*, 2022, **15**, 413–438.

29 Y. Gao, H. Raza, Z. P. Zhang, W. Chen and Z. H. Liu, *Adv. Funct. Mater.*, 2023, **33**, 18.

30 H. Su, J. Zhang, Y. J. Hu, Y. Y. Yao, X. X. Zheng, Y. T. She, B. X. Jia, L. L. Gao and S. Z. Liu, *Adv. Funct. Mater.*, 2023, **33**, 8.

31 L. Gao, X. T. Luo, J. L. Sun, Q. Li and Q. F. Yan, *Small*, 2023, **19**, 10.

32 Q. Zhang, Y. Zhao, X. Qin, M. Li, H. Sun, P. Zhou, W. Feng, Y. Li, J. Lu, K. B. Lin, L. Shi and Z. H. Wei, *Adv. Funct. Mater.*, 2024, **34**, 2308547.

33 M. Shirayama, H. Kadowaki, T. Miyadera, T. Sugita, M. Tamakoshi, M. Kato, T. Fujiseki, D. Murata, S. Hara, T. N. Murakami, S. Fujimoto, M. Chikamatsu and H. Fujiwara, *Phys. Rev. Appl.*, 2016, **5**, 25.

34 Z. J. Niu, W. F. Liu, K. X. Wang, W. W. Sun, X. A. Huo, Y. Q. Miao, T. T. You and P. G. Yin, *ACS Appl. Energy Mater.*, 2024, **7**, 3635–3644.

35 Q. Y. Wei, D. X. Zheng, L. Liu, J. S. Liu, M. Y. Du, L. Peng, K. Wang and S. Z. Liu, *Adv. Mater.*, 2024, **36**, 30.

36 M. Q. Wang, W. W. Wu, Y. L. Liu, S. Y. Yuan, D. H. Tian, C. L. Zhang, Z. P. Ma, J. H. Deng, J. H. Chen, Z. Z. Lou, W. Z. Li and J. D. Fan, *Adv. Funct. Mater.*, 2023, **33**, 13.

37 W. A. Dunlap-Shohl, Y. Y. Zhou, N. P. Padture and D. B. Mitzi, *Chem. Rev.*, 2019, **119**, 3193–3295.

38 Z. F. Wu, Z. H. Liu, Z. H. Hu, Z. Hawash, L. B. Qiu, Y. Jiang, L. K. Ono and Y. B. Qi, *Adv. Mater.*, 2019, **31**, 7.

39 D. Shi, V. Adinolfi, R. Comin, M. J. Yuan, E. Alarousu, A. Buin, Y. Chen, S. Hoogland, A. Rothenberger, K. Katsiev, Y. Losovyj, X. Zhang, P. A. Dowben, O. F. Mohammed, E. H. Sargent and O. M. Bakr, *Science*, 2015, **347**, 519–522.

40 J. S. Feng, X. J. Zhu, Z. Yang, X. R. Zhang, J. Z. Niu, Z. Y. Wang, S. N. Zuo, S. Priya, S. Z. Liu and D. Yang, *Adv. Mater.*, 2018, **30**, 9.

41 G. Wetzelaer, M. Scheepers, A. M. Sempere, C. Momblona, J. Avila and H. J. Bolink, *Adv. Mater.*, 2015, **27**, 1837–1841.

42 F. Zhang, D. Q. Bi, N. Pellet, C. X. Xiao, Z. Li, J. J. Berry, S. M. Zakeeruddin, K. Zhu and M. Grätzel, *Energy Environ. Sci.*, 2018, **11**, 3480–3490.

43 C. M. Wolff, P. Caprioglio, M. Stolterfoht and D. Neher, *Adv. Mater.*, 2019, **31**, 20.

44 Z. Li, X. Wu, B. Li, S. F. Zhang, D. P. Gao, Y. Z. Liu, X. T. Li, N. B. Zhang, X. T. Hu, C. Y. Zhi, A. K. Y. Jen and Z. L. Zhu, *Adv. Energy Mater.*, 2022, **12**, 10.

45 X. Li, F. Zhang, J. X. Wang, J. H. Tong, T. Xu and K. Zhu, *Nat. Sustain.*, 2021, **4**, 1038–1041.